Available online at www.sciencedirect.com
ScienceDirect
Journal of the European Ceramic Society 31 (2011) 2525–2534
www.elsevier.com/locate/jeurceramsoc

Simulation of micro powder injection moulding: Powder segregation and yield stress effects during form filling

Andreas Greiner[a,*], David Kauzlarić[a,b], Jan G. Korvink[a,b], Richard Heldele[c], Michael Schulz[c], Volker Piotter[c], Thomas Hanemann[c,d], Oxana Weber[c], Jürgen Haußelt[c,d]

[a] *Laboratory for Simulation, Department of Microsystems Engineering, University of Freiburg, Georges-Köhler-Allee 103, 79110 Freiburg, Germany*
[b] *School of Soft Matter Research, Freiburg Institute for Advanced Studies, University of Freiburg, Albertstr. 19, 79104 Freiburg, Germany*
[c] *Institute for Materials Research III, Karlsruhe Institute of Technology, Hermann-von-Helmholtz-Platz 1, 76344 Eggenstein-Leopoldshafen, Germany*
[d] *Laboratory for Materials Process Technology, Department of Microsystems Engineering, University of Freiburg, Georges-Köhler-Allee 103, 79110 Freiburg, Germany*

Available online 3 March 2011

Abstract

We report on our development of a computational tool for the simulation of micro powder injection moulding (micro-PIM) based on a description of the fluid flow by the smoothed particle hydrodynamics (SPH) method. The feedstocks used in micro-PIM expose rather complicated rheological features. Insertion of appropriate material models is discussed, as, *e.g.*, the yield stress behaviour. Insight is gained into the moulding process through simulation of the injection into a bending specimen with an obstacle in the flow as an example. The effect of shear induced migration is shown to be reproduced and compared to the segregation phenomena arising in experimental findings.
© 2011 Elsevier Ltd. All rights reserved.

Keywords: Injection moulding; Smoothed particle hydrodynamics; Simulation; Rheological models

1. Introduction

Besides the silicon-world of MEMS (micro electro mechanical systems), a great need exists for micro-structured polymers, metals, and ceramics. The application areas range from DNA analysis instruments in life science over biocompatible materials for medical applications to a variety of electronic devices for sensors and actuators. Micro powder injection moulding (micro-PIM) [1] is a popular process for the micro-structuring of pure polymers or polymeric feedstocks with ceramic or metallic particle load. In order to reduce production costs there is a need for predictive process simulation.

There are a variety of finite element(FE)-based simulation approaches.[2,3,4,5,6,7] A comparison of commercially available codes can be found in the work of Bilovol et al.[8] Usually, their disadvantage is the difficulty in handling free surfaces and large deformations. A meshless modeling is presented in Bernali et al. [9] for a Hele–Shaw flow in fluid injection in cavities.

On the other hand, particle-based approaches are able to deal with free surfaces and large deformations easily. Instead of meshing the domain, these methods subdivide the material itself into small portions ("particles") which are allowed to move relative to each other. In this work we apply the method smoothed particle hydrodynamics SPH [10,11,12] to the simulation of the micro-PIM process.

The simulation of casting with SPH was already successfully performed.[13,14] Here, we have to apply this method to materials, which are rheologically more complex. Therefore, we focus on two major effects occuring in the micro-PIM process leading to a high risk of failures or defects: the critical yield stress of the used feedstocks and the shear induced segregation of the embedded powder particles.[15,16,17]

Kwon and Park [18] considered the yield-stress in their filling simulations by extending the viscosity model and discovered a considerable effect on the clamping force. Alexandrou et al.[19] made a thorough analysis of inertial, viscous and yield-stress effects for a 1:5 expansion flow. For this geometrical set-up the biggest influence on the flow pattern that can be ascribed to the presence of a yield-stress was observed for Reynolds numbers larger than unity. In micro-PIM, the Reynolds numbers are generally smaller than unity. Nonetheless, in Section

* Corresponding author. Tel.: +49 761 2037384; fax: +49 761 203 7437.
E-mail address: andreas.greiner@imtek.uni-freiburg.de (A. Greiner).

0955-2219/$ – see front matter © 2011 Elsevier Ltd. All rights reserved.
doi:10.1016/j.jeurceramsoc.2011.02.008

7, we will be able to reproduce a complex filling pattern of the micro-PIM process by implementing a yield-stress model in the SPH-simulation.

For the injection moulding of powder filled feedstocks, a homogeneous distribution of powder particles is crucial in order to avoid cracks, porosity or distortions in the produced parts.[20] The extremely high shear rates of up to $10^6\ s^{-1}$ in micro-PIM may lead to powder binder segregation. This may lead to non-homogeneous binder extraction during the debinding step or to an anisotropic shrinkage during the sintering step resulting in cracks or deformations. Barriere et al.,[3] accounted for segregation in a FE-simulation by implementing a two phase model. In this work, we present a SPH-based approach describing the powder concentration as an internal degree of freedom. To this end we briefly discuss the respective equations of motion for the feedstock to be applied. The SPH discretisation of these equations of motion will be summarised together with a discussion of the boundary conditions for all degrees of freedom and their fluxes. A model for yield stress materials and for shear induced powder migration will be explained together with its tests and its application to relevant micro-PIM problems. For both cases the results are compared with experimental findings.

2. Governing equations of motion

The basic equations used for the description of the micro-PIM-process are the continuity equation for the density ρ

$$\frac{\mathrm{d}\rho}{\mathrm{d}t} = -\rho\nabla\cdot\mathbf{v} \tag{1}$$

where $\mathbf{v}$ is the velocity field vector, and the incompressible Navier–Stokes equation

$$\frac{\mathrm{d}\mathbf{v}}{\mathrm{d}t} = -\frac{\nabla P}{\rho} + \frac{1}{\rho}\nabla\cdot(\eta\nabla\mathbf{v}) \tag{2}$$

both given in a Lagrangian reference frame, with pressure P and viscosity η.

Notice the differences to the usual underlying equations of motion for finite element simulations: (i) For SPH, we require a description in the Lagrangian material frame of reference instead of the fixed in space Eulerian frame. (ii) Eq. (1) allows for density fluctuations instead of assuming strict incompressibility. (iii) In Eq. (2), incompressibility is approximated by a weakly compressible equation of state[21]

$$P(\rho) = P_0\left[\left(\frac{\rho}{\rho_0}\right)^{\gamma} - 1\right], \tag{3}$$

where $\gamma = 7$, ρ_0 is a reference density and $P_0 = c_s^2\rho_0/\gamma$, with the speed of sound c_s chosen large enough so that density fluctuations remain small.

3. SPH discretisation

The basis of SPH is the interpolation idea that an arbitrary function $f(\mathbf{r})$ of the position $\mathbf{r}$ may be expressed by [10,11]

$$f(\mathbf{r}) = \int f(\mathbf{r}')\, W(\mathbf{r}-\mathbf{r}')\, d\mathbf{r}' \tag{4}$$

where $W(\mathbf{r}-\mathbf{r}')$ is an interpolation function with finite support and its volume-integral is normalised to unity.

Given (4) a so-called finite interpolation method is introduced by replacing the integral by a sum over a finite set of points or "particles" distributed in space and $f(\mathbf{r})$ is replaced by the particle-centred value f_i, *i.e.*,

$$f_i = \sum_j \frac{m_j}{\rho_j} f_j W_{ij} \tag{5}$$

where m_j is the mass of the particle and ρ_j its associated local density. Additionally, $W_{ij} = W_{r_c}(\mathbf{r}_{ij})$ with $\mathbf{r}_{ij} = \mathbf{r}_i - \mathbf{r}_j$, and where $\mathbf{r}_i$ and $\mathbf{r}_j$ are the positions of particles i and j, respectively, and the width r_c of the interpolation function is of finite size.

Eq. (5) can be applied to directly compute the local density ρ_i around a particle i to read

$$\rho_i = \sum_j m_j W_{ij} \tag{6}$$

Note that the finite size of r_c makes the sum over j similar to the procedure applied in molecular dynamics, weighting the contributions of the neighbouring particles j to the interpolation within a cutoff radius r_c.

In order to represent derivatives like, *e.g.*, $(\nabla f)_i$ needed for the discretisation of (1) and (2), we apply (4) and (5) and integrate by parts to get

$$(\nabla f)_i = \sum_j \frac{m_j}{\rho_j} f_j \nabla W_{ij} \tag{7}$$

To compute the evolution of the densities ρ_i of the SPH-particles we discretise the equation of motion (1), *i.e.*,

$$\dot{\rho}_i = \sum_j m_j \mathbf{v}_{ij}\cdot\nabla W_{ij} = -\sum_j m_j \mathbf{v}_{ij}\cdot\mathbf{r}_{ij} w_{ij} \tag{8}$$

where we have set $\mathbf{v}_{ij} = \mathbf{v}_i - \mathbf{v}_j$ and $\nabla W_{ij} = -\mathbf{r}_{ij} w_{ij}$. In contrast to (6), this allows to simulate free surface flow.[21] The surfaces will be approximated to be stress-free. This, in combination with the equation of state (3), defining an initial reference density ρ_0 for each particle, results in a vanishing pressure at the free surface. The discretisation of the pressure gradient term in Eq. (2) reads

$$\frac{(\nabla P)_i}{\rho_i} = \sum_j m_j \left(\frac{P_i}{\rho_i^2} + \frac{P_j}{\rho_j^2}\right)\nabla W_{ij}. \tag{9}$$

This expression is anti-symmetric and therefore conserves linear and angular momentum exactly.

The discretisation of the viscous term in the momentum equation (2) reads[22]

$$\left[\frac{1}{\rho}\nabla\cdot(\eta\nabla\mathbf{v})\right]_i = -\sum_j m_j \frac{4\eta_i\eta_j}{\eta_i+\eta_j}\frac{w_{ij}}{\rho_i\rho_j}\mathbf{v}_{ij}. \tag{10}$$

This form takes care of strong local jumps in η.

4. Boundary conditions

Three types of boundaries are important: solid walls, inflows, and free surfaces of the material. For all boundary conditions at solid walls it is assumed that there is a layer of so-called boundary particles. This layer is situated outside of the domain of interest. It has a thickness of one support r_c of the used interpolation kernel, *i.e.*, the layer is built such that all created particles have at most a distance of r_c to the closest wall segment. The implementation of viscous forces near solid walls and near free surfaces have to be considered. For walls a no-slip condition is implemented by applying the technique of Morris et al.[23] which was extended to arbitrarily shaped mould wall geometries.[24] At free surfaces of the feedstock a stress free boundary condition is assumed.

We assume a no-slip condition even though slip at the walls is likely to occur.[25] The simulation results shown later show that the yield model leads to a reduction of the effective viscosity close to walls and to a slip effect which is very similar to the one of an explicit slip-layer model.[18] Nonetheless, the additional effect of slip on yielding and segregation should certainly be investigated in more detail in the future. Further experimental results not shown in this work, indicate that the yield stress effect presented here, also occurs in situations where slip may be definitely excluded.

For particle methods, inflow conditions for moving particles into non-periodic domains are usually realised by a reservoir and either a piston or a force representing gravity. The reservoir must contain enough particles in order to be able to fill the actual domain of interest which is initially empty. A computationally more efficient approach is briefly described in the following (details may be found in Kauzlarić[24]):

For the case of a constant inflow velocity initially, a regular layer of SPH particles is created. The particles are assigned the velocity v_{in} in inflow direction. The thickness of the layer in the inflow direction must be at least one kernel support r_c. Initially, these fluid particles move with their assigned constant velocity and do not interact with their neighbouring SPH particles. In the simplest case of a cubic lattice, with a layer of thickness r_c, after a time-period $\tau = r_c/v_{\text{in}}$ a new row of SPH particles is created. During their initial motion with the constant velocity v_{in}, the SPH particles pass a virtual barrier from which on they behave like usual SPH particles and exchange mass and momentum with their neighbours.

Besides the computational efficiency, a second advantage of this approach is that, in contrast to a piston, it indeed represents a constant inflow condition. Hence, the SPH-simulations can be easily compared to mesh based simulations where these kinds of boundary conditions are standard.

5. A model for yield stress

An important characteristic of most polymer-powder compounds is the observation of a critical yield-stress. Below this threshold, the material experiences no plastic deformation. Therefore a yield-stress model is implemented into the SPH-framework in this section.

Many powder-filled feedstock systems possess high viscosities leading to Reynolds numbers $Re<1$, especially for micro parts with small dimensions.[1] For this regime of Reynolds numbers, no matter whether yield-stress is considered or not, the so-called "mound-filling" pattern is observed for a 1:5 expansion flow in Alexandrou et al.[19]. But this does not permit the conclusion that the presence of a yield-stress is generally irrelevant for low Reynolds numbers. The motivation for including the yield-stress effect into the simulation of micro-PIM is the experimentally observed undesirable splitting effect in a channel with a cylindrical obstacle presented in Section 7.1.

5.1. Viscosity regularisation

A rigorous mathematical description of a yield-stress material is the Bingham model [26,27]. It states that

$$\boldsymbol{\tau} = \left(\eta_0 + \frac{\tau_y}{\dot{\gamma}}\right)\dot{\boldsymbol{\gamma}}, \quad \tau > \tau_y \tag{11}$$

$$\dot{\boldsymbol{\gamma}} = \mathbf{0}, \quad \tau < \tau_y \tag{12}$$

where $\boldsymbol{\tau}$ and $\dot{\boldsymbol{\gamma}} = \nabla\mathbf{v} + (\nabla\mathbf{v})^T$ are the extra-stress and strain rate tensors, respectively, and

$$\tau = \sqrt{\frac{1}{2}\boldsymbol{\tau}:\boldsymbol{\tau}}, \quad \dot{\gamma} = \sqrt{\frac{1}{2}\dot{\boldsymbol{\gamma}}:\dot{\boldsymbol{\gamma}}}, \tag{13}$$

represent the corresponding second invariants. The plastic viscosity of the yielded material is denoted as η_0.

This model strictly separates the material into a liquid domain with apparent viscosity $\eta_a = \eta_0 + \tau_y/\dot{\gamma}$ and a solid domain. Both domains are separated by the yield-surface defined through the points $\mathbf{r}_y$ where $\tau(\mathbf{r}_y) = \tau_y$.

To overcome the difficulties for unsteady flows and complex geometries due to the divergence of η_a for $\dot{\gamma}\to 0$, the discontinuity of the Bingham model and the interdependence of the yield-state and the velocity field, several modifications have been proposed that are continuous and applicable to both the yielded and unyielded domain simultaneously [28,29]. The basic idea of all these models is to replace Eq. (12) describing the solid domain by an expression for the stress τ in terms of a large viscosity. In this work the bi-viscosity model by O'Donovan and Tanner[28] is used which approximates Eqs. (11) and (12) by

$$\boldsymbol{\tau} = \left(\eta_0 + \frac{\tau_y}{\dot{\gamma}}\right)\dot{\boldsymbol{\gamma}}, \quad \dot{\gamma} > \dot{\gamma}_c \tag{14}$$

$$\boldsymbol{\tau} = \eta_s\dot{\boldsymbol{\gamma}}, \quad \dot{\gamma} \le \dot{\gamma}_c \tag{15}$$

Still, the stress is piecewise defined, but now, in terms of a critical shear rate $\dot{\gamma}_c$. The viscosity $\eta_s = \alpha\eta_0$ approximates the behaviour of the unyielded material, where $\alpha = 1 + \tau_y/(\dot{\gamma}_c\eta_0)$

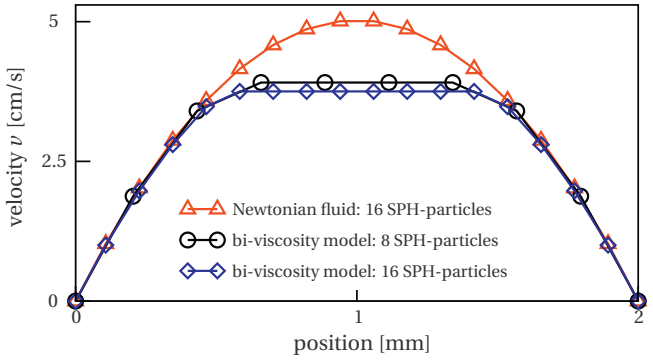

Fig. 1. Steady state solutions for Poiseuille flow with the bi-viscosity model for two different resolutions of 8 and 16 particles in the cross-section of width 2 mm. For comparison the velocity profile for the Newtonian case is shown as well. The symbols represent the simulation results, while the purpose of the lines is to guide the eye.

should be large enough or equivalently, $\dot{\gamma}_c$ should be small enough.

For the SPH-discretisation we have to take care since the viscosity is now a function of the shear rate $\dot{\gamma}$. Since it is in the nature of yield stress materials that yielded and unyielded domains are in close contact to each other, the effective viscosity can change rapidly in space. Therefore, the viscous interaction (10) is used, which allows for large differences in the transport coefficients η_i and η_j, in contrast to simpler discretisation approaches.[12]

We test the SPH-discretisation of the bi-viscosity model in a simulation of pressure driven Poiseuille flow between two parallel plates with a distance of 2 mm. The obtained steady state velocity profiles are shown in Fig. 1 for the two resolutions of 8 and 16 particles in the cross-section. For comparison, the Newtonian velocity profile for a resolution of 16 particles is also plotted.

The steady state solution is a partially yielded material. Due to the large difference in the viscosities of the yielded material and the unyielded material, the velocity profile in the unyielded domain is virtually flat as it should be for both resolutions. Just the transition zone between the yielded and the un-yielded material shows a curvature due to the smoothing properties of the SPH-discretisation and since the bi-viscosity model extends the ideal yield surface to a yield region.

6. A model for shear induced powder migration

Segregation will be described by a continuous mean particle density ϕ. This description will be correct as long as we may assume that a small fluid volume represented by one SPH-particle contains many powder particles. The validity of this assumption is a consequence of the used micrometer sized powders in micro-PIM.

We have chosen to implement the diffusive flux model by Philips et al.[30] into the SPH framework. This model is based on two diffusive fluxes $\mathbf{J}_c$ and $\mathbf{J}_\eta$ of a mean concentration of suspended particles ϕ. $\mathbf{J}_c$ includes the migration mechanisms due to local variations in the collision frequency of the suspended particles and reads

$$\mathbf{J}_c = -D_c a^2 \phi \nabla(\phi\dot{\gamma}) = -D_c a^2(\phi^2\nabla\dot{\gamma} + \phi\dot{\gamma}\nabla\phi) \tag{16}$$

since variations in the collision frequency are caused by concentration gradients $\nabla\phi$ and variations in the shear rate $\nabla\dot{\gamma}$. D_c is a diffusion constant and a is the particle diameter making the diffusion constant dimensionless. The diffusion constant has to be fitted experimentally and is therefore an empirical parameter.

In addition a spatially varying viscosity due to a spatially varying particle concentration can lead to an effective particle flux as well. The corresponding flux reads

$$\mathbf{J}_\eta = -D_\eta \dot{\gamma}\phi^2 \left(\frac{a^2}{\eta}\right) \frac{\partial\eta}{\partial\phi}\nabla\phi \tag{17}$$

where D_η is an empirical dimensionless rate constant.

Using both migration mechanisms the conservation equation for the volume fraction ϕ becomes

$$\frac{\partial\phi}{\partial t} = -\nabla\cdot(\phi\mathbf{v}) - \nabla\cdot(\mathbf{J}_c + \mathbf{J}_\eta) \tag{18}$$

The expression $\nabla\cdot(\phi\mathbf{v})$ covers the convective transport of the suspended particles.

Instead of discretising Eq. (18) directly, it is more convenient to use the equation of motion for the volume $V_\phi = \phi/\rho$ occupied by powder particles, where we have set the mass to $m = 1m^*$ for simplicity, *i.e.*, to the unit of mass m^* used in the simulation. The discretised equation for V_ϕ will be antisymmetric under exchange of fluid particles, which means exact volume conservation. Applying the SPH-discretisation formalism leads to[14]

$$\begin{aligned}\dot{V}_{\phi,i} = &-D_c a^2 \sum_j \frac{w_{ij}}{\rho_i\rho_j}(\phi_i+\phi_j)(\phi_i\dot{\gamma}_i - \phi_j\dot{\gamma}_j)\\ &- D_\eta a^2 \sum_j \frac{w_{ij}}{\rho_i\rho_j}\left(\dot{\gamma}_i\phi_i^2\left(\frac{\mathrm{d}\eta}{\eta\mathrm{d}\phi}\right)_i\right.\\ &\left.+\dot{\gamma}_j\phi_j^2\left(\frac{\mathrm{d}\eta}{\eta\mathrm{d}\phi}\right)_j\right)(\phi_i-\phi_j)\end{aligned} \tag{19}$$

For the dependence of the viscosity on the volume fraction we assume the Krieger rheological model[31] which is

$$\eta(\phi) = \eta_0\left(1 - \frac{\phi}{\phi_m}\right)^{-c}, \tag{20}$$

specifically with a saturation volume fraction of $\phi_m = 0.68$ and a scaling factor of $c = 1.82$. These values have been determined experimentally for hard spheres.[30] For a vanishing particle concentration the fluid has the reference viscosity η_0. The derivative with respect to ϕ becomes

$$\frac{1}{\eta}\frac{\partial\eta}{\partial\phi} = \frac{c}{\phi_m - \phi}. \tag{21}$$

6.1. Verification

The model is verified through computation of the concentration profile for Poiseuille flow to test the coupling to the flow field and to serve for a comparison to experimental results.

We analyze the migration of powder particles in pressure-driven Poiseuille flow between two parallel plates. The full set of equations is computed, *i.e.*, the time evolution of the velocity field is coupled to the evolution of the powder concentration (18) by the concentration dependence of the viscosity (20) and the dependence of the fluxes $\mathbf{J}_c$ (16) and $\mathbf{J}_\eta$ (17) on the shear rate $\dot{\gamma}$.

We choose $d_x = 250$ μm as the width of the cross-section in x-direction. This width corresponds to the experimental setup for which measurements from computer tomography (CT) are available.

The velocity component v_y is driven by a constant pressure gradient $p_y = 1.28$ MPa/cm which is implemented by applying an equivalent body-force on each SPH-particle in the periodic flow direction. The specific value depends on the resolution of the discretisation.

The particle diameter is taken to be $a = 9$ μm, the constant $D_c = 1.17 \times 10^9$ is chosen such that the time constant for reaching steady state is as small as possible and the ratio is $D_c / D_\eta = 0.6454$. The latter allows to compute an analytic solution for the steady state concentration profile for comparison.[30]

The simulation domain is discretised by SPH-particles which are initially at rest on a cubic lattice. The cross-section in x-direction is discretised with two different resolutions of 9 and 19 SPH-particles. For 19 particles, the viscosity range of approximately $[\eta(\phi_0), 1000\eta(\phi_0)]$ allows for a timestep of $\Delta t = 6.60 \times 10^{-12}$ ps.

The simulation is performed in 3D with periodic boundary conditions in the flow direction y and in z-direction. The x-direction is confined by solid boundaries. For the velocity no-slip boundary conditions are applied at the walls. For the concentration ϕ we assume that there is no flow across the boundaries. This is realised by forbidding any exchange of ϕ between the SPH-particles representing the liquid and the SPH-particles representing the solid walls.

Fig. 2 shows the profiles of the powder concentration, the velocity and the shear rate for steady-state. The analytic solution for the concentration is plotted as well.

Basically one can observe that the solid migrates to the centre of the channel and that the velocity profile is blunted. The latter is due to an increased viscosity in the centre because of the larger solids concentration. Consequently, the characteristic shear rate $\dot{\gamma}$ is no piecewise linear function anymore as it would have been for a parabolic velocity profile. As a consequence there is a back coupling of the powder migration on the flow behaviour. This shows that it is crucial to add the degree of freedom ϕ describing the powder concentration. By just estimating the powder migration from the shear fields it is not possible to account for its effect on the rheology.

A comparison of the computed concentration with the analytic solution shows that the computed result does not fully reach $\phi = \phi_m = 0.68$ at the peak. The reason is the smoothing of the SPH interpolation. As a consequence, due to mass conservation, the concentration at the walls is larger than $\phi = 0.45$ as would have been expected from the analytic solution. It can be seen that the error decreases when increasing the resolution from 9 to 19 particles in the cross-section.

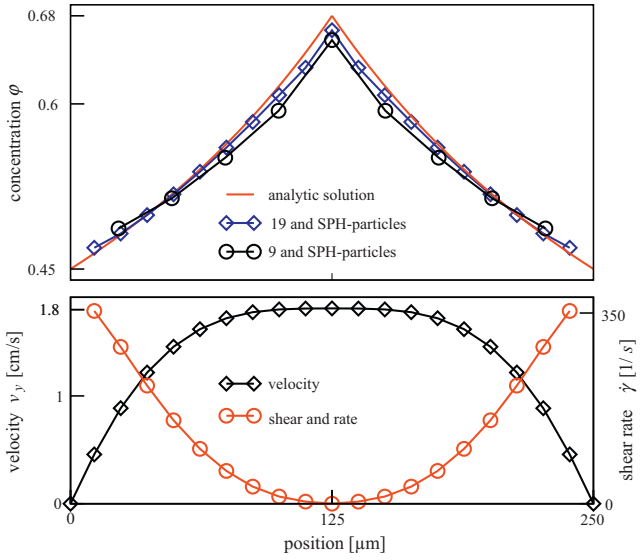

Fig. 2. Steady state powder concentration for Poiseuille flow. Along with the analytic solution the top graph shows the computed powder concentration for discretisations with 9 and 19 SPH-particles in the cross-section. The bottom graph shows the computed profiles of the flow velocity and the shear rate. The symbols represent the values of the corresponding SPH-particles while the lines are for guiding the eye.

6.2. Poiseuille flow vs. CT-measurement

In order to compare with the experiment we choose $\eta_0 = 33.2$ Pas, $\phi_m = 0.794$ and $c = 0.714$ for the Krieger model (20). One obtains a "mean" viscosity $\eta(\bar{\phi}) = 100$ Pas, where $\bar{\phi} = 0.625$ and the pressure gradient p_y accelerates the SPH-particles to a velocity of the order of centimeters per second (cf. Fig. 2), which is a realistic value for the micro-PIM process. The values for $\bar{\phi}$, ϕ_m, $c = 0.7014$ and $\eta(\bar{\phi})$ have been obtained from viscosity measurements.[17] The remaining simulation parameters are kept the same as in Section 6.1.

Fig. 3 shows the transient evolution of the powder concentration as obtained from the simulation and, below, a measurement of powder segregation by computer tomography (CT). Here, a polyethylene/wax based feedstock with a steel powder (average particle diameter 6.6 μm) was used. The large particle diameter was necessary for the CT. The compounding and the feedstock properties are well described in Refs. [15,32].

In the simulation, steady state of the velocity profile is reached after $t \approx 1.98$ μs $= 300$t* where t* ≈ 6.6 ns is the unit of time of the simulation. The concentration profile reaches steady state after $t \approx 0.99$ μs. Fang and Phan-Thien[33] observed that the velocity equilibrates faster. In the simulations presented here, the equilibration of ϕ was boosted by purpose by choosing large constants D_c and D_η.

Segregation starts close to the walls and propagates towards the centre where, around $t = 7$t* a cusp starts to grow. Around

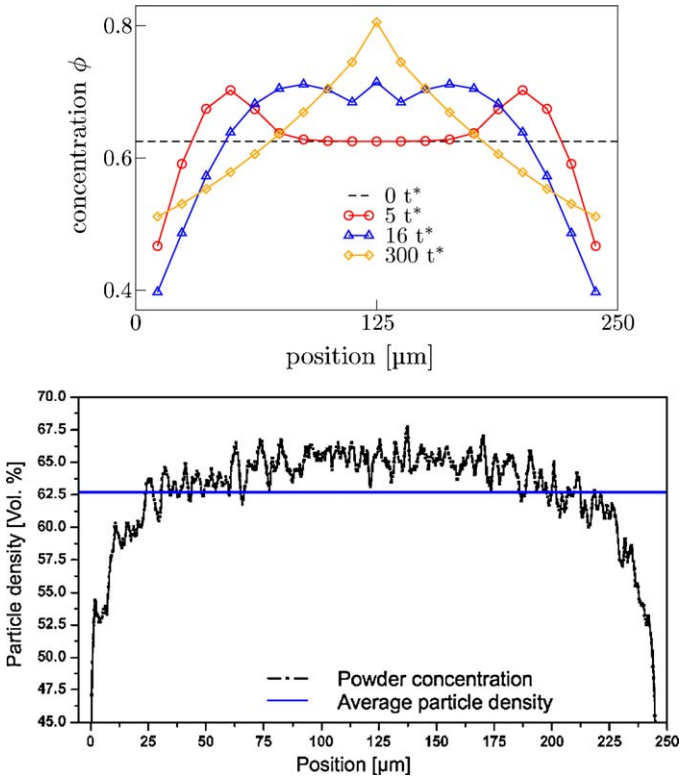

Fig. 3. (Top) Transient evolution of the powder concentration for Poiseuille flow. The time is given as multiples of the time unit $t^* = 1000\Delta t = 6.6$ ns. The graph on top shows the evolution of the concentration profile until the steady state is reached at $t \approx 300t^*$. The results were obtained with 19 SPH-particles in the cross-section. The symbols represent the values of the corresponding SPH-particles while the lines are for guiding the eye. (Bottom) CT-measurement of powder segregation.[17]

$t = 16t^*$ the profile has certain similarities with the experimental results [17] shown in Fig. 3 below. This indicates that steady state might never be reached during the micro-PIM process, *i.e.*, the longer the channel, the larger the segregation. This implies that a quantitative reproduction of the experiment in terms of correct time scales requires a reduction of the absolute values of D_c and D_η in the simulation.

In contrast to the one-dimensional profile obtained from the simulation, the CT-measurements were performed for a quadratic cross-section. In addition, the flow situation in the experiment is not as well defined as in the simulation. The first reason is that the injection gate is relatively close to the location of the measured cross-section. Additionally the flow-history of the material before taking the CT-snapshot is not well known, including the time, the material experienced considerable shear rates leading to the observed segregation.

Nonetheless a qualitative comparison between the simulation and the centre-line of the quadratic cross-section is possible. For a quantitative comparison and a quantitative determination of the coefficients D_c and D_η, the timescales of the flow history must be determined. The exact ratio D_c/D_η can be determined by the measurement of a quasi-stationary situation,[30] which is admittedly difficult for the micro-PIM process. Pressing the feedstock through long capillaries and measuring the concentration profile

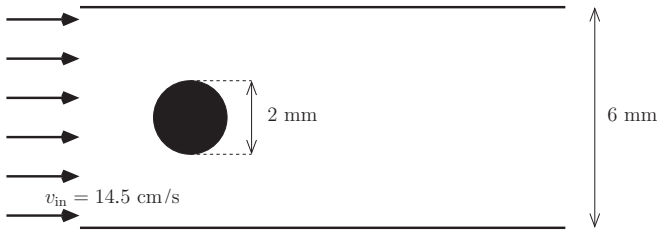

Fig. 4. Geometry considered for the filling simulation. The feedstock is assumed to enter the domain with a constant uniform velocity v_{in}.

for cross-sections at different locations along the length might deliver the required results.

It is worth to mention, that a peak close to the centre of a rectangular channel was observed as well in CT-measurements.[17] It is too early to start to interpret this as the peaks observed in the Phillips model and it is worth to enlarge the amount of measured CT-data in order to be able to make assured statements which go beyond the proof that migration in a channel is directed towards the centre.

We wish to strongly emphasise that Fig. 2 shows a steady-state situation for $t \to \infty$ which will never be observed in the experiment. For a comparison with the experiment, the intermediate profile from Fig. 3 should be considered, which is quite close to the measurements. The intermediate profiles usually show a weaker segregation than the steady state. Nonetheless it is significant. An even better quantitative agreement was obtained by optimising the ratio of the Phillips parameters D_c and D_η, which is shown elsewhere.[34]

7. Case studies

We present two case studies in this section, one applying the yield-stress model, and one applying the powder migration model, respectively. Section 7.1 shows the reproduction of the experimental observation which was the motivation for the incorporation of a yield-stress model, namely the splitting of a feedstock filling a channel with a cylindrical obstacle. Section 7.2 illustrates the effects of powder segregation in a mould geometry of complex shape.

7.1. Yielding around a cylinder: experiment and simulation

The relevance of the inclusion of a yield-stress model and the qualitative correctness of the chosen approximation by an effective shear rate dependent viscosity is demonstrated by reproducing an observation from micro-PIM experiments. The relevant characteristics of the geometry are shown in Fig. 4.

Fig. 5(a) and (b) visualise the filling pattern for two different powder concentrations of the used feedstock by images of parts resulting from partial filling.[17] The feed rate was kept constant at $\dot{V} = 4\ \text{cm}^3/\text{s}$ in both experiments. The details of the feedstock are given in Ref. [32].

The temperature of the feedstock was 140°C. The temperature of the mould in the experiment was set to 50°C [35], while the simulation was isothermal at the feedstock temperature. This is most likely the explanation for the detachment of the feedstock

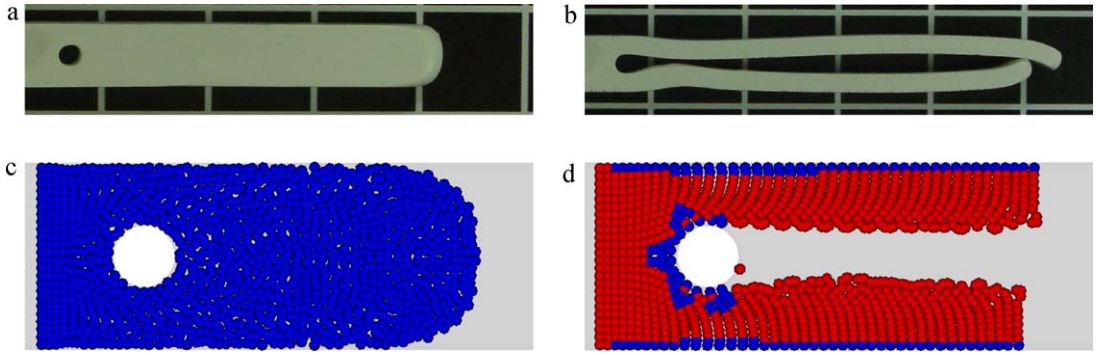

Fig. 5. Application of the yield-stress model from Section 5 to the filling of a geometry with cylindrical obstacle. Figures (a) and (b) show the experimentally obtained filling patterns for feedstocks with a powder concentration of 40 vol.% and 55 vol.%, respectively. Total mould volume: $V = 2.4\ \mathrm{cm}^3$. Feed rate: $\dot{V} = 4\ \mathrm{cm}^3/\mathrm{s}$. Figures (c) and (d) show the simulations with a small and a large effective yield-stress, respectively. Blue SPH-particles indicate yielded material with low effective viscosity while red particles indicate unyielded material with large effective viscosity. (For interpretation of the references to color in this figure legend, the reader is referred to the web version of the article.)

from the mould wall as observed in the experiment but not in the simulation (cf. Fig. 5), where it would have to be modelled by more complex boundary conditions. The detachment of the feedstock from the mould wall seems to be an effect of the cooling down of the feedstock. Preliminary experimental results for a mould wall temperature equal to the feedstock temperature of 140°C do not show any detachment but still the splitting effect at the cylindrical obstacle.

While an intuitively expectable shape is obtained for a powder concentration of 40 vol.%, a permanent splitting of the flow front is observed for a powder concentration of 55 vol.%.

Note that this large variation of solid content was indeed possible for the used feedstock. At both powder concentrations, the feedstock was well characterisable and the mould filling under the chosen process parameters was possible. Of course the material properties of the produced part may be very different. But here, the only purpose of the large variation of the powder concentration was the comparison of mould filling experiments with the results of the filling simulations of the yield stress model.

It is known from measurements that the yield stress of the feedstock increases with the powder concentration.[17] Hence, in Fig. 5(b) the fraction of unyielded material might have increased leading to the observed change in the filling pattern.

This hypothesis is tested by SPH-simulation and by application of the yield-stress model from Section 5. We concentrate on the yielding behaviour of the material since we believe it to suffice for the explanation of the observed splitting effect. Therefore additional shear-thinning of the feedstock at large shear rates is ignored.

The experimental results presented in Fig. 5(a) and (b) basically show a 2D-effect. Therefore it is legitimate to reduce the simulation to a 2D-problem as shown in Fig. 4. The total width of 6 mm is resolved by 24 SPH-particles in order to obtain a resolution of at least eight SPH-particles for the 2 mm gaps.

The inflow condition is approximated by a constant inflow-velocity of the SPH-particles, *i.e.*, by a Dirichlet boundary condition $v_{\mathrm{in}} = 14.5\ \mathrm{cm/s} = \mathrm{const.}$ on the left boundary of the rectangular 2D-domain (cf. Fig. 4). The velocity v_{in} is chosen as in the experiment.

The upper and lower boundaries represent walls of the mould geometry. Additionally there is a cylindrical obstacle in the centre of the channel, and a wall far-off at the right end. At all walls we assume a no-slip condition $\mathbf{v}_w = \mathbf{0}$ even though slip at the walls is likely to occur.[25] The simulation results in Fig. 5(d) show that the yield model leads to a reduction of the effective viscosity close to walls and to a slip effect which is very similar to the one of an explicit slip-layer model.[18]

For low shear rates, the flow viscosity of the used feedstock is of the order of $\eta_0 = 1000$ Pas.[17] Therefore, assuming a shift of the effective viscosity of three orders of magnitude for the modelling of the unyielded regime requires a maximum viscosity of $\eta_s = 10^6$ Pas for the simulation.

For a width of $h \approx 250\ \mu\mathrm{m}$, η_s, and the mass density $\rho = 3200\ \mathrm{kg/m}^3$ we can estimate the allowed integration time step Δt to be of the order of 10^{-11} s. For a process time of the order of hundreds of milliseconds, this leads to unacceptably long simulation times for the currently applied time-integration algorithm. The algorithmic optimisation is beyond the scope of this work. Therefore, we solve this problem with a scaling argument as follows.

For the size of the two dimensional system regarded here, $\Delta t \geq 10^{-6}$ s is still acceptable in order to get computing times in the order of hours on a single processing unit. In terms of the Reynolds number $Re = \rho v d/\eta$, we get $Re(\eta_s) \approx 10^{-7}$ and $Re(\eta_0) \approx 10^{-4}$. It can be expected that, as long as we remain in the laminar flow regime, increasing the Reynolds number should not spoil the yield-effect we wish to observe. Increasing Δt by five orders of magnitude to the feasible $\Delta t = 10^{-6}$s gives $Re'(\eta_0') \approx 10^1$, which is still in the range of laminar flow. This can be achieved by decreasing the viscosities to $\eta_0' = 10^{-2}$ Pas and $\eta_s' = 10$ Pas. Hereby we preserve the ratio $\eta_s/\eta_0 = \eta_s'/\eta_0' = 1000$.

The bi-viscosity model (15) is used with these two effective viscosities as the parameters for the description of the unyielded and yielded domain. Two simulations are performed where the critical shear rate describing the transition between the unyielded and the yielded domain is set to $\dot{\gamma}_c = 0\ \mathrm{s}^{-1}$ and $\dot{\gamma}_c = 0.9\ \mathrm{s}^{-1}$, respectively. The latter was estimated by moni-

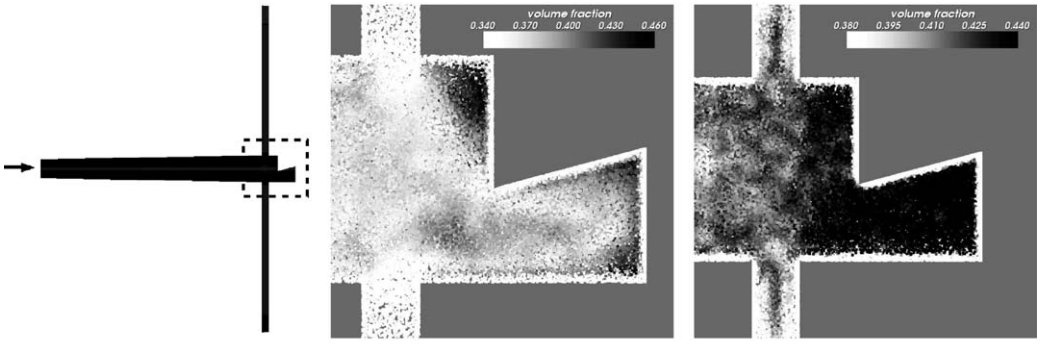

Fig. 6. Segregation in a complex geometry. (a) Test geometry for the simulation of the injection process. (b) Solids load in an early stage of the mould filling. (c) Solids load in a later stage.

toring the shear rates of the first simulation with $\dot{\gamma}_c = 0\ \mathrm{s}^{-1}$, *i.e.*, of the completely Newtonian liquid with $\eta = \text{const.}$. For $\dot{\gamma}_c = 0.9\ \mathrm{s}^{-1}$, a coexistence of yielded and unyielded domains should be observed.

Fig. 5(c) and (d) shows the resulting flow patterns for $\dot{\gamma}_c = 0\ \mathrm{s}^{-1}$ and $\dot{\gamma}_c = 0.9\ \mathrm{s}^{-1}$, respectively. Blue SPH-particles possess a low effective viscosity close to η_0' while red particles represent domains with large effective viscosity closer to η_s'. In (d), the expected coexistence of yielded and unyielded domains can be observed. Simultaneously, the flow pattern changes considerably and is in accordance with the experimental findings shown in figures (a) and (b). This effect may also coincide with segregation phenomena as the binder segregation will be higher in the high shear regions and thus the tendency to yield in these regions is higher. Hence, combining the yield stress model and the powder migration model, should be a next step following the work presented in this paper.

In Fig. 5 (d) one can observe that the yielded regime is very narrow and concentrated to the regions close to the walls of the mould where the highest shear rates occur. The shear planes have less viscous contact close to the walls leading to a slip-like effect. As a consequence the bulk material slides along a quasi slip-layer. In the interior of the bulk material the shear planes have a strong viscous contact leading to an almost negligible interior deformation. The viscous contact between the shear planes in the Newtonian case in figures (a) and (c) is more homogeneous. Therefore, the observed filling pattern corresponds to the one observed for Newtonian liquids. The introduction of shear thinning is expected to lead to only minor deviations from the Newtonian behaviour because the change of the viscosity is less steep than in a yield-stress model.

One might argue that the observed one-particle layer in Fig. 5 (d) could as well be a numerical artifact. Two facts support the result is physical. First, it was observed that increasing the particle resolution, increases the number of particles in the layer. Second, near the cylinder, *i.e.*, at the region with the largest shear rates, the yielded layer with low viscosity gets thicker, even for the given low resolution. Examining directly the shear rates (not shown here) also shows reasonable values. The value of the viscosity is just the consequence of the values of the shear rate. Nonetheless, more detailed convergence studies by varying the particle resolution would be useful.

For the flow pattern observed in Fig. 5 (d) a coexistence of yielded and unyielded material is essential. The recommendation to the process engineer is therefore to avoid such a flow situation, at least for the presented geometry. In practice this means to either increase the shear rates by increasing the feed rate, or to reduce the critical yield-stress by decreasing the powder concentration. An optimal compromise has to be found because, on the other hand, increasing the feed rate will lead to a larger segregation of the solid fraction (cf. Section 6) while a lower powder concentration complicates the debinding and sintering processes.[36] Modifications of the binder chemistry can help to optimise the rheology without changing the solids load.[17]

7.2. Segregation in a complex geometry

As a more complex application of the powder migration model from Section 6 we consider the simulation of injection moulding into a test geometry as depicted in Fig. 6(a). We concentrate on the region marked by the dashed rectangle. The arrow indicates the gate of the mould geometry and the flow direction.

Fig. 6(b) is a snapshot of an early stage of the injection. In this stage, the velocity field in the volume directly behind the gate is still inhomogeneous, *i.e.*, there is a strong shear field. The distribution of the solids load indicates an aggregation at convex corners (*i.e.*, pointing into the mould material) and a decrease at concave corners (*i.e.*, pointing into the cavity). This is intuitively understandable since the shear rate in the proximity of convex corners should be lower than in the bulk of the geometry. On the other hand, concave corners are regions of large shear rates.

In later stages of the filling, the flow in the volume close to the gate becomes more homogeneous and directed towards the two arms at the top and the bottom. In these arms strong shear rates occur since they are very narrow. The effect can be seen in Fig. 6(c). The concentration in the part of the entrance volume behind the two arms is rather homogeneous and large. The concentration in the front part is a few percent lower since this is the region where the feedstock is still flowing towards the arms and undergoes shearing motion. Inside the arms the average

concentration is even lower. This indicates that a larger fraction of the solid particles prefers to stay in the entrance volume where shear rates and flow velocities are lower. Additionally, the solids load has a maximum in the centre of the arms as already observed earlier for flow in a channel.

It should be noticed that, in the presented simulations, we did not consider full or partial solidification of the material. This is the reason why the inhomogeneities from Fig. 6(b) are able to disappear or are replaced by other types of inhomogeneities. If the material solidified at least partially in the entrance region, *e.g.*, in the right part, the inhomogeneous solids load would be frozen in. In the worst case, all observed inhomogeneities could occur simultaneously, eventually leading to cracks or deformations during the sintering step.

8. Summary and discussion

An SPH-framework was developed which allows to simulate the injection process of micro powder injection moulding (micro-PIM). As shown, the simulations are not limited to academic problems but can be performed in arbitrarily complex geometries. For this purpose, boundary conditions used in SPH have been generalised to be applicable in a domain which is bounded by flat arbitrarily arranged wall segments. In addition, an efficient inflow boundary condition was developed which omits the usage of large particle reservoirs and pistons.

Two major effects in micro-PIM, effects due to an inherent yield stress and shear induced powder migration were investigated. A yield-stress material was modelled by means of the bi-viscosity [28] approach.

The simulations successfully reproduce partially yielded steady state velocity profiles as well as an experimental observation of splitting in a channel with cylindrical obstacle.

Shear induced powder migration was incorporated by means of Phillips' diffusive flux model.[30] This model was discretised by formulating an SPH-equation of motion for the occupied volume V_ϕ with exact pairwise conservation properties. The simulations correctly predict powder migration to regions with the lowest shear rates. For injection moulding into complex geometries the simulations help to predict an accumulation of the solids fraction at convex corners (pointing outside of the cavity) and a depletion at concave corners (pointing inside the cavity). For a quantitative matching of the transport coefficients D_c and D_η of the Phillips model we suggest CT-measurements of the powder-concentration for well defined geometries such as long capillaries.

This work has focussed on two crucial effects, namely, yielding and segregation. We have certainly not presented a complete model for the whole process. Further investigations should combine the yield-stress model and the powder migration model into one simulation to observe combined effects. For this purpose, experimental data from Ref. [17] should be incorporated that relates the yield stress directly to the powder concentration. In addition, slip and freezing at the walls should be considered. The latter is likely to suppress the segregation phenomena slightly but not totally, as we see from the experiment, which shows strong demixing at the walls as well. For the yielded material, the bi-viscosity-model with its constant viscosity is of course too simple and shear-thinning should be added on top of the yield-stress model to make the rheological behaviour more realistic. But it was already tested that shear-thinning alone cannot reproduce the observed splitting effect. Also the Phillips model for powder migration is the simplest which one can take and certainly it has its practical and mathematical flaws, for example a cusp in the steady state that, in the form observed in the Phillips model, is unphysical, but, in a rounded form, may be realistic. There are numerous improvements of the Phillips model [37,38,39,40,41,42] that can be implemented in our SPH-model if needed. But it is by far more important to investigate this need by producing more experimental data first.

Acknowledgements

The authors wish to express their gratitude to the Deutsche Forschungsgemeinschaft (DFG) for funding of this project in the framework of the Sonderforschungsbereich Mikrourformen (SFB499).

References

1. Baltes H, Fedder GK, Hierold C, Korvink JG, Tabata O. In: *Microengineering of metals and ceramics. Advanced micro and nano systems.* Weinheim: Wiley-VCH; 2005.
2. Bilovol VV, Kowalski L, Duszczyk J. Numerical simulation of the powder injection moulding process for optimization of mould design and process parameters. *Adv Eng Mat* 2000;**2**(3):127–31.
3. Barriere T, Gelin JC, Liu B. Experimental and numerical investigations on properties and parts produced by MIM. *Powder Metall* 2001;**44**(3):228–34.
4. Barriere T, Gelin J, Liu B. Improving mould design and injection parameters in metal injection moulding by accurate 3D finite element simulation. *J Mat Proc Technol* 2002;**125**(Sp Iss SI):518–24.
5. Barriere T, Liu B, Gelin J. Determination of the optimal process parameters in metal injection molding from experiments and numerical modeling. *Mat Proc Technol* 2003;**143**(Sp. Iss. SI):636–44.
6. Cheng Z, Barriere T, Gelin J. A new explicit simulation for mould filling with high viscous feedstock. *Acta Mech Solida Sinica* 2004;**17**(4):347–52.
7. Cheng Z, Barriere T, Gelin J. A new explicit simulation for injection molding and its validation. *Polym Eng Sci* 2009;**49**(6):1243–52.
8. Bilovol V, Kowalski L, Duszczyk J, Katgerman L. Comparison of numerical codes for simulation of powder injection moulding. *Powder Metall* 2003;**46**(1):55–60.
9. Bernal F, Kindalan M. RBF meshless modeling of non-Newtonian Hele–Shaw flow. *Eng Anal Boundary Elem* 2007;**31**(10):863–74.
10. Gingold RA, Monaghan JJ. Smoothed particle hydrodynamics: theory and application to non-spherical stars. *Mon Not R Astr Soc* 1977;**181**: 375–89.
11. Lucy LB. A numerical approach to the testing of the fission hypothesis. *Astron J* 1977;**82**(12):1013–24.
12. Monaghan JJ. Smoothed particle hydrodynamics. *Rep Progress Phys* 2005;**68**:1703–59.
13. Ha J, Cleary PW. Simulation of high pressure die filling of a moderately complex industrial object using smoothed particle hydrodynamics. *Int J Cast Met Res* 2005;**18**:81–92.
14. Kauzlarić D, Lienemann J, Pastewka L, Greiner A, Korvink JG. Integrated process simulation of primary shaping: multi scale approaches. *Microsys Technol* 2008;**14**:1789–96.
15. Heldele R, Rath S, Merz L, Butzbach R, Hagelstein M, Hausselt J. X-ray tomography of powder injection moulded microparts using synchrotron radiation. *Nucl Instrum Methods Phys Res B* 2006;**246**:211–6.

16. Heldele R, Schulz M, Kauzlarić D, Korvink JG, Hausselt J. Micro powder injection molding: process characterization and modeling. *Microsys Technol* 2006;**12**:941–6.
17. Heldele R. *Entwicklung und Charakterisierung von Formmassen für das Mikropulverspritzgießen*. Ph.D. thesis; University of Freiburg; 2008.
18. Kwon TH, Park JB. Finite element analysis modeling of powder injection molding filling process including yield stress and slip phenomena. *Polym Eng Sci* 1995;**35**:741–53.
19. Alexandrou AN, Duc E, Entov V. Inertial, viscous and yield stress effects in Bingham fluid filling of a 2d cavity. *Non-Newtonian Fluid Mech* 2001;**96**:383–403.
20. Wei WCJ, Tsai SJ, Hsu KC. Effects of mixing sequence on alumina prepared by injection molding. *J Euro Ceram Soc* 1998;**18**:1445–51.
21. Monaghan JJ. Simulating free surface flows with SPH. *J Comp Phys* 1994;**110**:399–406.
22. Cleary PW, Monaghan JJ. Conduction modelling using smoothed particle hydrodynamics. *J Comp Phys* 1999;**148**:227–64.
23. Morris JP, Fox PJ, Zhu Y. Modeling low reynolds number incompressible flows using SPH. *J Comp Phys* 1997;**136**:214–26.
24. Kauzlarić D. Particle simulation of MEMS/NEMS components and processes—theory, software design and applications. *microsystem simulation, design and manufacture, IMTEK Freiburg, vol. 1*. Tönning: Der Andere Verlag; 2009.
25. Kalyon DM, Yaras P, Aral B, Yilmazer U. Rheological behavior of a concentrated suspension: a solid rocket fuel simulant. *J Rheol* 1993;**37**:497–523.
26. Bingham EC. *Fluidity plasticity*. New York: McGraw-Hill; 1992.
27. Oldroyd JG. A rational formulation of the equations of plastic flow for a Bingham solid. *Proc Camb Philos Soc* 1984;**15**:75–83.
28. O'Donovan EJ, Tanner RI. Numerical study of the Bingham squeeze film problem. *J Non-Newtonian Fluid-Mech* 1984;**15**:75–83.
29. Papanastasiou TC. Flows of materials with yield. *J Rheol* 1987;**31**:385–404.
30. Phillips RJ, Armstrong RC, Brown RA, Graham AL, Abbott JR. A constitutive equation for concentrated suspensions that accounts for shear-induced particle migration. *Phys Fluids A* 1992;**4**(1):30–40.
31. Krieger IM. Rheology of monodisperse lattices. *Adv Colloid Interface Sci* 1972;**3**(2):111–36.
32. Heldele R, Schulz M, Hausselt J. Detection of powder-binder separations during micropim by synchrotron computer tomography. In: *Proceedings of the PM 2008 World Congress*. 2008.
33. Fang Z, Phan-Thien N. A particle suspension model: an unstructured finite-volume impleentation. *J Non-Newtonian Fluid Mech* 1999;**80**: 135–53.
34. Kauzlarić D, Pastewka L, Meyer H, Heldele R, Weber O, Piotter V, et al. SPH-simulation of shear induced powder migration in injection moulding. *Phil Trans Royal Soc A*; in press.
35. Piotter V, Beck M, Ritzhaupt-Kleissl HJ, Ruh A, Haußelt J. Recent developments in micro ceramic injection molding. *Int J Mat Res* 2008;**99**: 1157–62.
36. German RM, Bose A. *Injection molding of metals and ceramics*. Princeton, NJ: Metal Powder Industries Federation; 1997.
37. Tetlow N, Graham AL, Ingber MS, Subia SR, Mondy LA, Altobelli SA. Particle migration in a Couette apparatus: experiment and modeling. *J Rheol* 1998;**42**:307–27.
38. Ingber MS, Graham AL, Mondy LA, Fang Z. An improved constitutive model for concentrated suspensions accounting for shear-induced particle migration rate dependence on particle radius. *Int J Multiphase Flow* 2009;**35**:270–6.
39. Mills P, Snabre P. Rheology and structure of concentrated suspensions of hard spheres. Shear induced particle migration. *J Phys II France* 1995;**5**:1597–608.
40. Morris JF, Boulay F. Curvilinear flows of noncolloidal suspensions: the role of normal stresses. *J Rheol* 1999;**43**:1213–37.
41. Miller RM, Morris JF. Normal stress-driven migration and axial development in pressure-driven flow of concentrated suspensions. *J Non-Newtonian Fluid Mech* 2006;**135**:149–65.
42. Kauzlarić D, Greiner A, Korvink JG. A non-local extension of the Phillips model for shear induced particle migration. *J Microsys Technol*; in press.